Research Square

Preprints are preliminary reports that have not undergone peer review.
They should not be considered conclusive, used to inform clinical practice,
or referenced by the media as validated information.

Ultra Compact Spaceborne Computational Single Photon 3D Imaging Based on Temporal Coding and Co-aperture Active-Passive Fusion

Bo Liu

boliu@ioe.ac.cn

Chinese Academy of Sciences https://orcid.org/0000-0003-3084-0126

Youfu Xu

Beijing Institute of tracking and telecommunication technology

Mei Zhou

Aerospace Information Research Institute, Chinese Academy of Sciences

Song Gao

Laser Fusion Research Center, China Academy of Engineering Physics

Jingyu Liao

Institute of Optics and Electronics, Chinese Academy of Sciences

Yun Jiang

Institute of Optics and Electronics, Chinese Academy of Sciences

Jie Li

Institute of Optics and Electronics, Chinese Academy of Sciences

Guang Guo

Chinese Academy of Sciences

Guanglin Liu

Institute of Optics and Electronics, Chinese Academy of Sciences

Bin Zhao

Chinese Academy of Sciences https://orcid.org/0000-0002-2959-3968

Hanlin Yang

Institute of Optics and Electronics, Chinese Academy of Sciences

Fengyun Huang

Institute of Optics and Electronics, Chinese Academy of Sciences

Yuqiang Yang

Institute of Optics and Electronics, Chinese Academy of Sciences

Jian Hu

Aerospace Information Research Institute, Chinese Academy of Sciences

Haohao Wu

Aerospace Information Research Institute, Chinese Academy of Sciences

Huijing Zhang

Aerospace Information Research Institute, Chinese Academy of Sciences

Dong Su

Laser Fusion Research Center, China Academy of Engineering Physics

Xiongwei Yan

Laser Fusion Research Center, China Academy of Engineering Physics

---

Article

Keywords: spacebarne single-photon LiDAR, multi-beam, temporal coding, active-passive fusion, co-aperture, 3D imaging

Posted Date: July 24th, 2026

DOI: https://doi.org/10.21203/rs.3.rs-9963566/v1

License: This work is licensed under a Creative Commons Attribution 4.0 International License. Read Full License

Additional Declarations: There is **NO** Competing Interest.

Ultra Compact Spaceborne Computational Single Photon 3D Imaging Based on Temporal Coding and Co-aperture Active-Passive Fusion

Bo Liu[123]*, Youfu Xu[4], Mei Zhou[5], Song Gao[6], Jingyu Liao[12], Yun Jiang[12], Jie Li[1], Guangmeng Guo[1], Guanglin Liu[1], Bin Zhao[123], Hanlin Yang[1], Fengyun Huang[1], Yuqiang Yang[1], Jian Hu[5], Haohao Wu[5], Huijing Zhang[5], Dong Su[6], Xiongwei Yan[6]

Affiliations:

1. Institute of Optics and Electronics, Chinese Academy of Sciences, Chengdu 610209, China.
2. State Key Laboratory of Light Field Manipulation Science and Technology, Chengdu 610209, China.
3. University of Chinese Academy of Sciences, Beijing 100049, China.
4. Beijing Institute of tracking and telecommunication technology. Beijing 10083, China
5. Aerospace Information Research Institute, Chinese Academy of Sciences, Beijing 100094, China
6. Laser Fusion Research Center, China Academy of Engineering Physics, Mianyang 621900, China

*E-mail: boliu@ioe.ac.cn

Abstract

High-resolution, wide-swath, and all-weather 3D Earth observation is of paramount significance for Earth system science, carbon cycle monitoring, disaster response, and fine-scale topographic mapping. However, scaling traditional spaceborne LiDAR systems toward multi-beam, high-repetition-rate, and multi-modal fusion configurations is fundamentally bottlenecked by range ambiguity, intense solar background noise, and the stringent size, weight, and power (SWaP) constraints associated with separated active and passive payloads. Here, we demonstrate an ultra-compact spaceborne multi-beam single-photon LiDAR 3D imaging system (UCSMSPL) that integrates computational temporal coding with co-aperture active–passive fusion, and present its detection results acquired in-orbit. Despite stringent payload resource constraints (~0.18 m³, 117 kg, and 490 W), the system successfully demonstrated in-orbit parallel single-photon earth observation with 36 independent detection channels. Its co-aperture dichroic design provides a parallax-free, hardware-level 1:40 spatial correspondence between the 1064 nm single-photon ranging channels and a 1440-pixel visible-light CCD array. By combining computational photonic temporal coding with cross-correlation decoding, the payload further enables direct in-orbit retrieval of absolute target elevations (with a calibrated precision of 0.15 m). By synergizing optical system integration with computational photonics, this work demonstrates high-density, low-power, multi-modal 3D remote sensing on a micro-satellite platform, establishing a new paradigm for real-time, constellation-based 3D Earth observation.

Keywords: spacebarne single-photon LiDAR, multi-beam, temporal coding, active-passive fusion, co-aperture, 3D imaging

1. Introduction

Acquiring high-precision, high-spatiotemporal resolution 3D digital topographies of the Earth's surface holds irreplaceable scientific value in domains such as carbon cycle monitoring, polar glacier dynamics analysis, and fine-scale topographic mapping [1-8]. Traditional passive or semi-active remote sensing methods primarily capture surface radiation, texture, and scattering features, but inherently struggle to directly obtain 3D geometric structures and vertical elevation information [9-11]. Light Detection and Ranging (LiDAR), by actively emitting high-repetition-rate short optical pulses and measuring the echo time-of-flight (TOF), directly establishes the geometric relationship between the payload and the target. It has thus emerged as a critical tool for transitioning from 2D remote sensing to comprehensive 3D Earth cognition [12-14].

Early spaceborne LiDAR systems were predominantly built upon linear detection regimes. Relying on echo energy amplitude measurements and continuous waveform reconstruction, these systems have played a pivotal role in monitoring ice sheets, sea ice, vegetation canopies, and terrestrial elevations [15-18]. However, as mission demands increasingly shift toward high-revisit rates, dense spatial sampling, and deployment on resource-constrained platforms, the fundamental limitations of the linear regime, particularly in weak echo detection, high-repetition rate sampling and system miniaturization have become increasingly apparent.

Subsequently, Single-Photon LiDAR (SPL) emerged as a disruptive active remote sensing technology. By time-tagging discrete photon events, the single-photon detection regime pushes the ranging sensitivity limit down to the single-photon level. This drastically reduces the required energy per pulse, thereby enabling higher repetition rates and significantly denser spatial sampling [19-24]. NASA's Advanced Topographic Laser Altimeter System (ATLAS) payload, aboard the ICESat-2 satellite, successfully demonstrated the remarkable capabilities of micro-pulse photon-counting spaceborne platforms in acquiring global elevation data. This milestone marked a revolutionary transition in spaceborne LiDAR technology, shifting the paradigm from "traditional waveform energy measurement" to "discrete quantum statistics."

However, scaling single-photon detection systems toward higher observational dimensions—such as massive multi-beam arrays and multi-modal optical image fusion—while drastically miniaturizing the payload for low-cost micro-satellite constellations, poses formidable physical challenges and engineering bottlenecks (for context, ATLAS provides only 6 parallel beams and weighs nearly 300 kg) [25-31]. As SPL technology attempts to further expand toward multi-beam, wide-swath, and multi-modal fusion architectures, three core bottlenecks remain [31-35]. First, the severe range ambiguity introduced by high-repetition-rate emittings fundamentally limits unambiguous measurement distances. Second, intense solar background noise during daytime observations severely compresses the effective dynamic range of single-photon systems, a challenge that is particularly pronounced in the visible-light spectrum [22-24]. Third, traditional active laser altimeters and passive imaging cameras are typically mounted as physically separated units. The structural thermal deformations and attitude jitter inevitably introduce spatiotemporal parallax driven by physical separation. This makes the stable, reliable fusion of 3D elevation and 2D texture information highly dependent on complex, computationally heavy post-processing registration [34, 35]. Furthermore, the stacking of such independent payloads inevitably leads to a massive surge in system volume and weight (typical spaceborne systems often weigh hundreds of kilograms), precluding their deployment on agile micro-satellite platforms [25-31].

To address these challenges, we developed and successfully validated in-orbit an ultra-compact spaceborne computational single-photon 3D imaging system that overcomes these key bottlenecks. Operating under extremely stringent Size, Weight, and Power (SWaP) constraints (120 kg, 0.18 m^3, 490 W), the proposed system successfully achieves 36-beam parallel detection in low Earth orbit (LEO). To the best of our knowledge, this represents the highest number of parallel beams for any active Earth observation laser payload currently operating in-orbit worldwide. By constructing a co-aperture active-passive dichroic architecture and integrating innovative computational photonic temporal coding technology within the space environment, this system enables, for the first time, all-time, real-time 3D terrain extraction directly in-orbit. More importantly, the system demonstrates an unprecedented active-passive, photon-level hardware fusion capability in space, directly outputting zero-parallax fused 3D surface data with visible-light imagery natively in-orbit. The results reported herein establish a systematic

application template and provide a critical technological demonstration for the next generation of spaceborne single-photon LiDAR systems.

2. System Architecture and Main Parameters

Figure 1 illustrates the overall optical configuration of the UCSMSPL. The system utilizes a synergistic co-aperture fusion architecture for both active laser ranging and passive visible-light imaging. It is composed of a time-encoded laser transmitting unit, a co-aperture receiving telescope, a dichroic imaging module, a 36-channel fiber-coupled single-photon detection module, a Time-to-Digital Converter (TDC) unit, and an electronics main control unit.

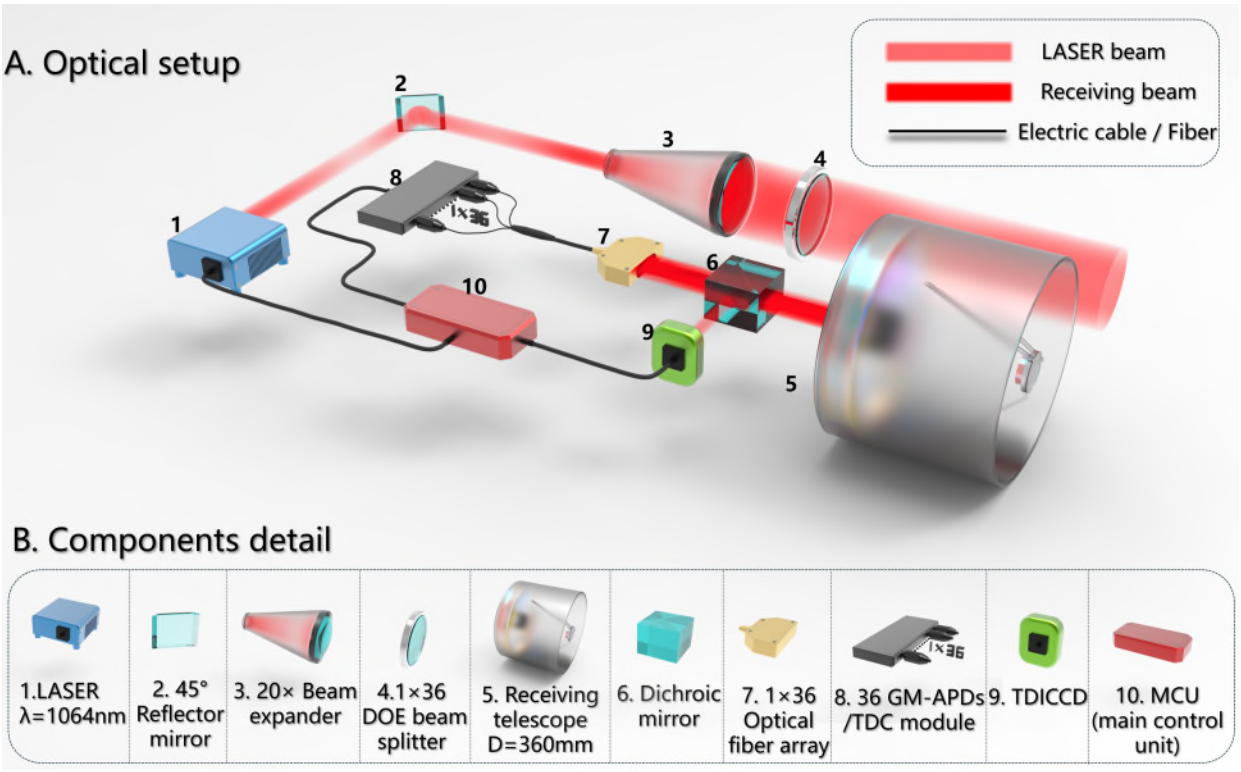


Figure 1. Optical architecture of the UCSMSPL. (a) 1064 nm laser light is reflected by a mirror, expanded by a beam expander and split by a DOE to a 1 × 36 beam array. The target echo is collected by the receiving telescope and coupled into the fiber array, and then detected by 36 GM-APDs, while the visible light is received by the TDICCD. (b) Components detail.

At the transmitter side, time-encoded 1064 nm laser pulse sequences are generated and subsequently reflected by a 45° mirror into a 20× beam expansion system. Post-expansion, the

laser beam diameter is increased to approximately 120 mm to suppress the beam divergence angle and enhance the uniformity of the far-field energy distribution. The expanded laser then passes through a Diffractive Optical Element (DOE) beamsplitter, where it is partitioned into 36 sub-beams of approximately uniform energy. These sub-beams are characterized by an angular spacing of approximately 150 μrad, forming a linear 1 × 36 parallel laser array directed toward the ground. The divergence angle of each individual sub-beam after expansion is approximately 20 μrad, resulting in a series of equidistant laser footprints on the ground perpendicular to the orbital flight direction. Each sub-pulse carries total transmitting energy of 10 mJ, which is uniformly distributed among the 36 transmitting beams by the DOE.

At the receiver end, the weak signal photons backscattered from terrestrial targets are collected by a 360 mm aperture telescope and focused near a shared focal plane. A dichroic beamsplitter is positioned near this focal plane to facilitate spectral separation between the active laser echoes and the passive visible-light signals. The visible-light band is directed to a 1440 pixel Time-Delay Integration CCD (TDICCD) detector to acquire passive imagery that is strictly field-matched with the laser ranging channels. Simultaneously, the 1064 nm laser echoes are channeled into a 1 × 36 optical fiber end-face array. Located precisely at the focal plane of the laser echoes, the 36 fiber end-faces correspond to the 36 laser receiving fields of view (FOVs), achieving a one-to-one spatial correspondence with the 36 transmitting beams.

Each receiving fiber is equipped at its exit end with a collimating microlens and a narrowband interference filter (center wavelength: 1064.2 nm; bandwidth: 0.5 nm) to effectively suppress solar background noise and out-of-band stray light. The filtered signals are then reconverged by micro-optical lenses onto the active areas of the single-photon detectors. The detection module comprises 36 discrete silicon-based Geiger-mode avalanche photodiodes (GM-APDs) with photon detection efficiency (PDE) of approximately 3% at 1064 nm. The echo pulses generated by the detectors are fed directly into the TDC unit for timing. The instantaneous field of view (IFOV) for each receiving channel is 80 μrad—four times the divergence angle of the corresponding transmitting beam. This configuration provides a robust tolerance margin for platform micro-vibrations, thermal-induced structural deformations, and atmospheric-induced beam pointing jitter, while concurrently minimizing the acquisition of

background noise photons. The primary technical parameters of the system are summarized in Table 1.

Table 1 Main system parameters

Laser wavelength	1064.2 nm
Laser repetition rate	20 kHz (sub-pulse) 125 Hz (macro-pulse)
Beam number	1 × 36
Laser sub-pulse energy	10/36 mJ
Sub−beam laser divergence	20 μrad
Sub-beam angular spacing	150 μrad
Receiving aperture	0.36 m
Sub-beam receiving FOV	80 μrad
Ranging accuracy	0.15 m
Orbit altitude	~400 km
Power consumption	490 W
Payload weight	117 kg

To achieve high-precision matching between the transmitting and receiving optical axes, the 45° mirror is mounted on a piezo-driven, two-dimensional precision steering mechanism, enabling precise closed-loop adjustment of the laser beam pointing. This design dynamically compensates for alignment tolerances, thermally induced deformations, and in-orbit slight pointing deviations, ensuring that all 36 transmitting beams fall accurately into their respective receiving FOVs.

Managing 36 parallel single-photon channels within a highly miniaturized footprint presents formidable electronic and optical crosstalk challenges. Traditional monolithic focal plane arrays (FPAs) are extremely susceptible to false triggering between adjacent channels, primarily driven by avalanche luminescence. To overcome this, we implemented a spatially decoupled, high-precision fiber routing mechanism—effectively "breaking the whole into parts." At the separated 1064 nm focal plane, an ultra-compact 36-core optical fiber array is deployed to extract the weak echoes from the 36 beams and physically guide them to 36 independently packaged GM-APDs.

This physical isolation fundamentally establishes a 36-beam crosstalk-free parallel single-photon detection network. Unlike monolithic FPAs, the optical fiber medium physically severs the pathways for carrier diffusion and avalanche emission, yielding absolute zero optical crosstalk between adjacent channels, while providing excellent stray light suppression capability. More crucially, this independent packaging enables the system to exert precise, localized control over the thermoelectric cooling (TEC) and bias voltage for each individual GM-APD. This decoupled architecture guarantees the operational consistency and long-term stability of the UCSMSPL. Collectively, these innovative designs lay a robust physical foundation for the extraction of weak photons against intense solar backgrounds.

A major engineering hurdle for this system lay not only in the optical fusion of 36-beam single-photon ranging and visible-light imaging but also in densely packing all functional units into a cubic payload frame of approximately 0.5 m × 0.6 m × 0.6 m. To meet the stringent volume, weight, rigidity, and optical-axis stability constraints imposed by small spaceborne platforms, the system employs a monolithic titanium alloy load-bearing frame. The whole payload frame was meticulously optimized through an integrated opto-mechanical-thermal design and fabricated as a single piece via high-precision metal 3D printing. Within a highly constrained space, it simultaneously provides a highly stable optical mounting reference, high-efficiency thermal management, and maximum structural rigidity and thermal stability, this design provides the critical assurance needed for the long-term, precise matching of the 36 transmitting beams with their corresponding receiver FOVs in complex orbital environments. The 3D model and physical photographs of the UCSMSPL payload are presented in Figure 2.

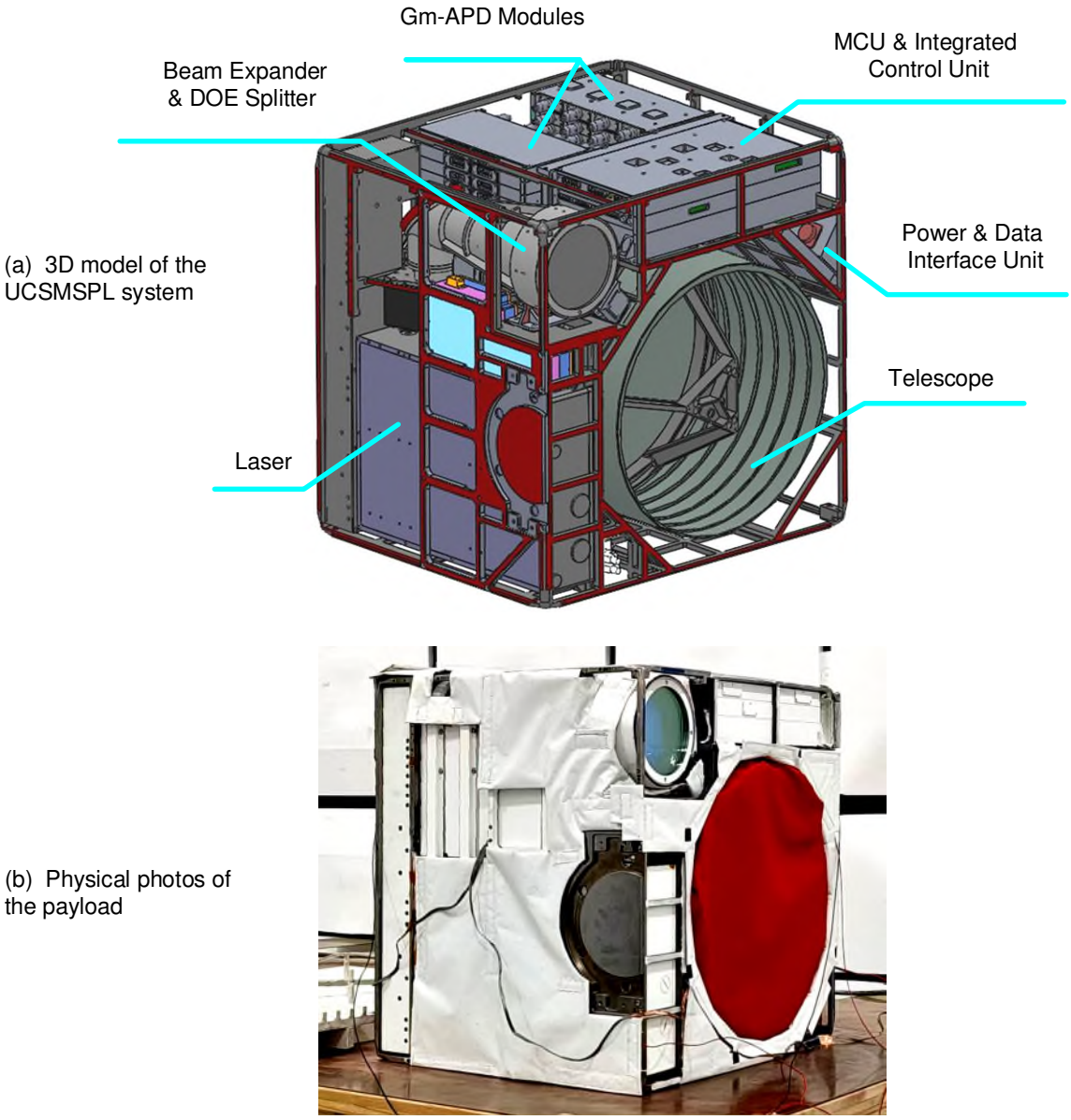


Figure 2. 3D model and photographs of the UCSMSPL payload

The homologous visible-light imaging and laser ranging co-aperture photonic architecture brings about an absolutely locked 1:40 hardware-level spatial mapping. Such fixed spatiotemporal coherence ensures that the laser echo photons and visible imaging photons experience identical fore-optics distortions and platform attitude perturbations. This implies that the geomorphological textures acquired by the payload in-orbit naturally carry their corresponding elevation data. This pixel-level hardware fusion thoroughly eliminates the

necessity of post-processing computational registration. Schematic diagram of the multi-beam single photon LiDAR detection was shown in Fig.3

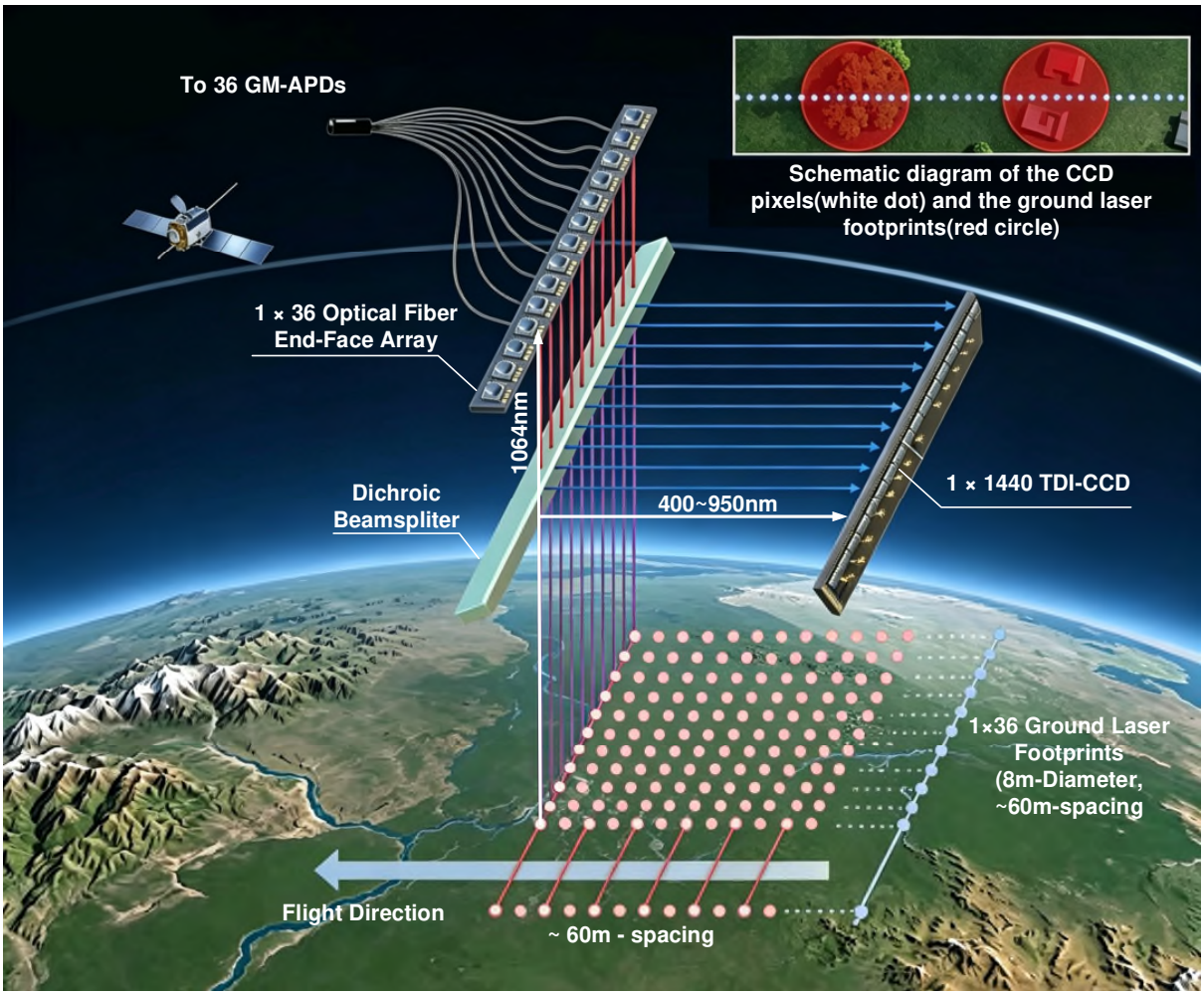


Figure 3. Schematic diagram of the UCSMSPL detection. The system uses a dichroic beamsplitter for echo spectral separation, where the 1064 nm signal enters the single-photon detection channel, and the 400-950 nm signal enters the visible-light detector array. Concurrently, a 1×36 ground laser footprint is formed for 3D surface detection.

3. In-orbit real-time data processing

In photon-counting LiDAR, high-repetition-rate emitting can improve photon sampling efficiency per unit time, but it also causes adjacent pulse echoes to overlap on the time axis, thereby introducing range ambiguity. To solve this problem, this study introduces a computational temporal coding modulation-demodulation scheme into the spaceborne single-

photon LiDAR, translating the range ambiguity problem in high-repetition-rate ranging into a correlation decoding problem of photon statistical sequences in the temporal domain.

Distinct from conventional equal-time-interval transmitting schemes, the UCSMSPL defines the basic observation window as a macro-pulse period of 8 ms, corresponding to a repetition frequency of 125 Hz. Within each macro-pulse period, the laser is modulated to continuously emit 20 sub-pulses, corresponding to an equivalent sub-pulse repetition rate of up to 20 kHz. The core characteristic is that the time intervals of these 20 sub-pulses present a non-uniform staggered distribution: they start from 49.1 μs and linearly increment to 50.9 μs with extremely high time-control precision.

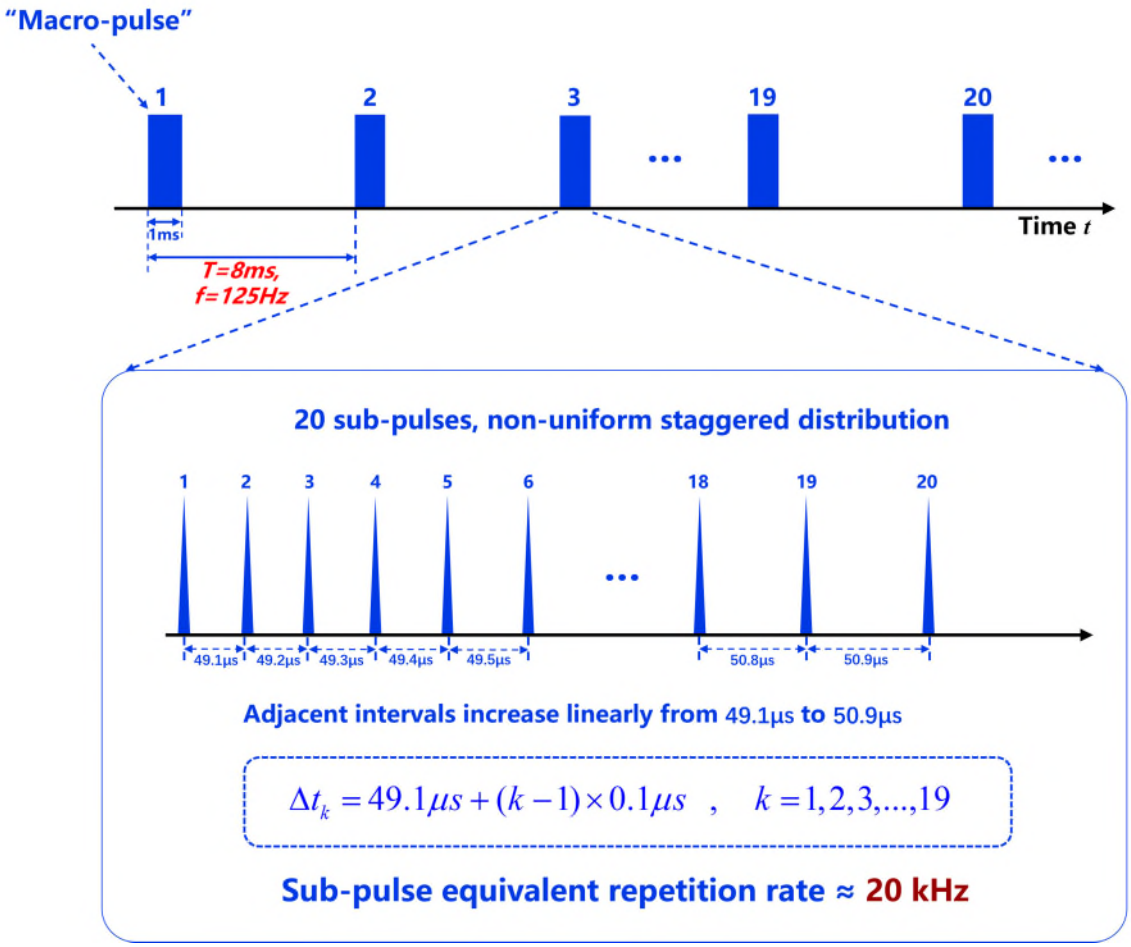


Figure 4: Schematic diagram of macro/sub-pulse temporal coding.

This meticulously designed ascending time sequence essentially injects a unique "orthogonal temporal signature" into each photon stream at the transmitting end. At the receiving end, the single-photon detector captures a discrete Poisson process composed of a very small number of true signal photons, a massive amount of solar background photons, and dark

counts. The spaceborne MCU executes continuous cross-correlation computation in-orbit, convolving the time histogram containing all photon arrival time-tags with the known transmitting template function. Since environmental noise follows a random uniform distribution on the time axis, its cross-correlation result will only produce a flat, low baseline; whereas only the signal photons that have experienced the true TOF—whose intrinsic time intervals strictly conform to the 49.1~50.9 μs increment law—can be coherently enhanced in the time-domain cross-correlation, exciting a highly SNR-advantaged dominant Delta-like peak at the true absolute flight distance.

In the k-th macro-pulse period, the photon arrival events recorded by the single-photon detector are discretized into a time histogram $H_k(t)$. This histogram, jointly composed of sparse true target echo photons, abundant solar background photons, and detector dark counts, can be expressed as:

$$H_k(t) = H_s(t) + H_n(t)$$

Where $H_s(t)$ is the contribution of target echoes and $H_n(t)$ is the solar background photon and dark count contribution. Since background photons and dark counts approximate a uniform Poisson process within the observation time window, their time distribution lacks deterministic correlation with the transmitting coding template, thus primarily manifesting as a low-amplitude, nearly flat background baseline in the correlation decoding output.

Assuming the template function corresponding to the known sub-pulse transmitting sequence is $S(t)$, the time bin width is u, and the delay search index is α, the candidate TOF delay is αu. The discrete cross-correlation between the receiving histogram and the transmitting template can be defined as:

$$R(au) = \sum_t H_k\,(t + au)S(t)$$

By traversing different delay indices α, the matching degree between the received photon events and the local transmitting template at different candidate TOFs can be obtained. For true target echoes, their temporal structure can be approximated as a delayed version of the transmitting template $S(t)$ by the target TOF τ. Therefore, when the search delay satisfies αu=τ, the received echo sequence and the local template reach optimal alignment on the time axis, and the cross-correlation output produces a significant main peak. The target TOF can be obtained through peak searching:

$$a_{\text{peak}} = \arg\max_a R(au)$$

and the corresponding peak TOF is

$$\tau_{\text{peak}} = a_{\text{peak}} u$$

further considering the system's fixed optoelectronic delay τ_0, the target range can be expressed as:

$$R_{\text{target}} = \frac{c}{2}\left(\tau_{\text{peak}} - \tau_0\right) = \frac{c}{2}\left(a_{\text{peak}} u - \tau_0\right)$$

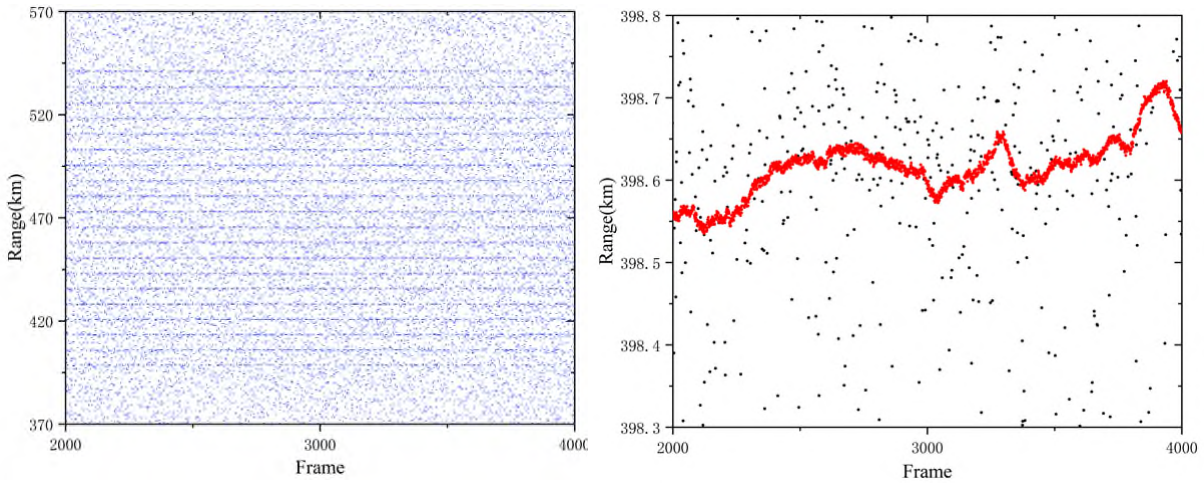
where c is the speed of light in a vacuum.

Unlike conventional equal-interval sub-pulse transmitting schemes, this method adopts a non-uniform incrementally spaced time sequence of 49.1~50.9 μs, giving each macro-pulse a unique temporal signature internally. This aperiodic coding effectively disrupts the periodic structure of the template's autocorrelation function, dispersing side lobe energy to different delay positions, thereby suppressing distance ambiguity caused by periodic transmitting. Only the true echoes that strictly maintain this incremental time interval feature can coherently accumulate in the cross-correlation output and form a main peak; while random background photons and dark counts do not meet this temporal coding law and cannot produce a stable correlation peak.

Therefore, this temporal coding and cross-correlation decoding mechanism can achieve robust recovery of absolute TOF and unambiguous ranging under strong solar background and detector dark count conditions. This computational demodulation method enables the system to directly and unambiguously lock onto the target elevation amid massive background noise in-orbits up to 400 km, using a single detection channel and extremely low laser transmitting power. Pre-launch vacuum optical delay calibration strictly verified that the intrinsic ranging precision of this temporal coding architecture at the instrument end reached 0.15 m, fully meeting the requirements for high-precision 3D Earth observation.

4. In-Orbit Data Results

After the payload was launched into orbit, it commenced in-orbit operation and debugging in July 2025, subsequently acquiring a massive amount of high-precision detection data.



(a) Raw point cloud data from one channel (b) Compensated reconstruction results

Figure 5. (a) Raw point cloud from one channel, which containing a large number of discrete noise photons, and showing 20 ground echo trajectories formed by 20 time-coded sub-pulses; (b) Compensated reconstruction results based on computational temporal coding and cross-correlation template matching.

Figure 5 shows a typical distribution of raw photon point clouds from one channel acquired in the sunlit region of orbit, along with the compensated reconstruction results. The horizontal axis represents the macro-pulse index (frame number), with an adjacent point ground spacing of about 60 m, and the vertical axis is the ranging value. The algorithm performs cross-correlation template matching on the raw photon events, compensates the signal photons—which satisfy the 49.1~50.9 μs incremental time interval law—back to their initial TOF positions, and obtains the final ranging values. The figure shows that under the noise background in daytime, the cross-correlation main peak based on the sub-pulse sequence still maintained a high signal-to-noise ratio of 10.6 dB, and the authentic terrestrial envelope is clearly distinguishable (the red curve is the final topographic ranging result).

Regarding the system's unique active-passive fusion detection capability, the most direct performance demonstration comes from scanning results over typical high-relief mountainous terrains on Earth.

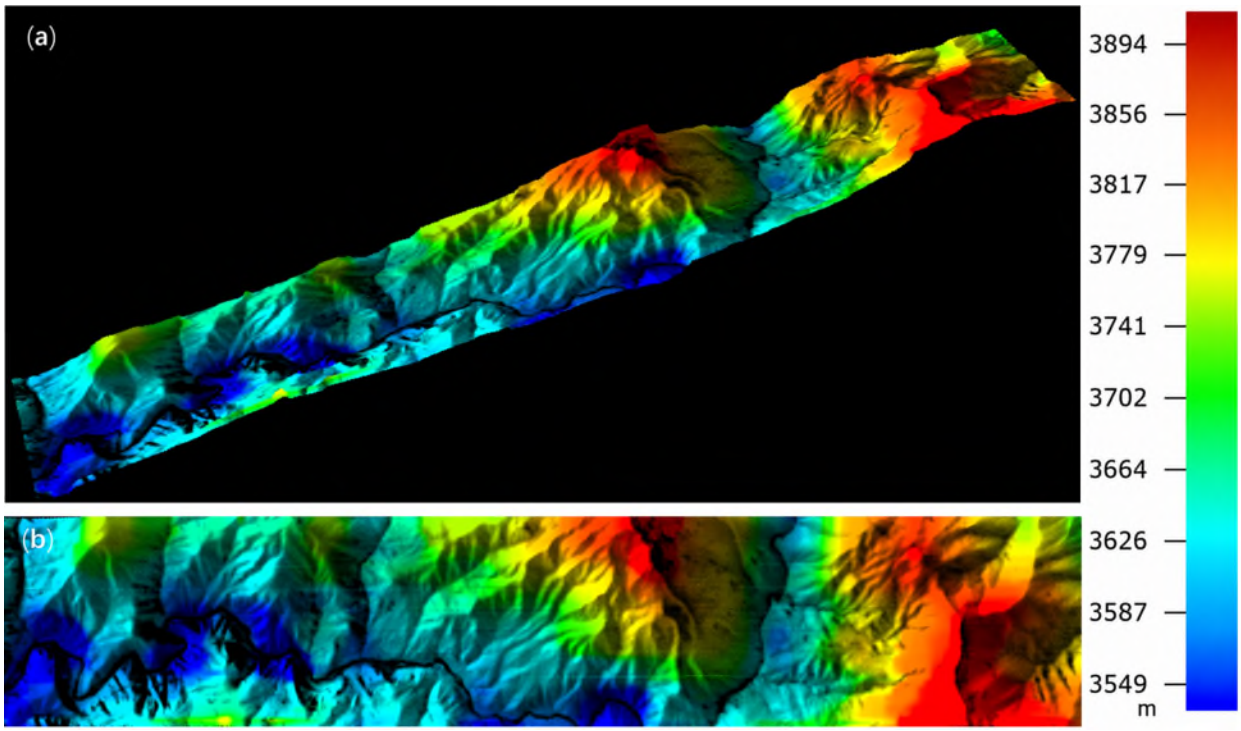


Figure 6. 3D terrain reconstruction results of the single-photon LiDAR. (a) Topographic point cloud/digital elevation model reconstruction result from a 3D perspective, with colors representing target elevation. (b) 2D overhead elevation map of the corresponding area, used to display topographic undulations, valley structures, and local detail distribution. The right color bar indicates elevation values in meters, with an overall elevation range of approximately 3549~3894 m.

Figure 6 presents a colorized fused 3D elevation topographic map directly generated in-orbit by the system. The image utilizes a 1.5-meter resolution visible-light texture from the 1440-pixel CCD as the base layer, seamlessly overlaid with 60m×60m grid laser ranging data that has been strictly hardware-mapped at a 1:40 ratio. Benefiting from the parallax-free characteristic brought by the co-aperture design, the figure displays an extremely smooth and precise surface morphology tracking capability: from sharply undulating mountain ridges to deep V-shaped canyons, the color transitions of the color textures (e.g., exposed rock areas and vegetation-covered areas) exhibit pixel-level perfect alignment with elevation cliffs.

Even if drastic topographic changes cause the photon TOF to experience high-frequency jumps within the millisecond level, the computational temporal coding algorithm still demonstrates extremely strong robustness, without the appearance of any ghosting artifacts or elevation discontinuities caused by pulse aliasing. The significance of this result lies not only in obtaining 3D point clouds, but also in the fact that the 3D information intrinsically carries the corresponding visible-light texture tags at the very source of data acquisition, thereby

significantly shortening the traditional heterogeneous data post-processing registration chain. For complex surface scenarios, this direct fusion capability is expected to enhance the stability and application efficiency of multi-modal product generation. This result indicates that the single-photon point cloud after temporal coding compensation can recover continuous terrain structures and achieve large-scale surface 3D morphology characterization.

5. Discussion

The ultra compact co-aperture computational photonic architecture presented herein demonstrates that, under strict volume, weight, and power constraints, a spaceborne single-photon LiDAR can simultaneously achieve multi-beam parallel detection, active-passive zero-parallax fusion, and unambiguous ranging at high repetition rates.

By executing the macro/sub-pulse demodulation computation at the pre-stage FPGA hardware layer, the system directly downlinks high-confidence elevation and fused images, significantly saving the highly valuable satellite-to-ground communication bandwidth. Although the currently employed silicon-based GM-APDs have not yet reached the ultimate limits in photon detection efficiency (PDE, ~3%), slightly limiting penetration depth over ultra-low reflectivity polar or deep-water regions, the established system architecture represents the optimal physical trade-off for miniaturized spaceborne active optics.

Methodologically, the co-aperture design shortens the error propagation chain between active and passive information; the fiber routing and independent APD packaging enhance the controllability and consistency of multi-channel systems; and the temporal coding provides a robust solution for absolute ranging under high PRF conditions without significantly increasing opto-mechanical complexity.

This synergistic "optical integration - detection isolation - computational decoding" mechanism establishes a new implementation pathway for miniaturized, high performance active 3D remote sensing payloads. Moving toward application scenarios, the successful operation of this payload clears the engineering and technical hurdles for deploying large-scale, low-cost LEO 3D remote sensing constellations. It holds great promise to shift the paradigm of 3D Earth observation from a "low-revisit, heavy post-processing" mode to a "high-revisit, strong-fusion, real-time-processing" era.

Data availability

The in-orbit data that support the findings of this study are available from the corresponding author upon reasonable request and subject to mission data-release policy.

Code availability

The decoding and processing code used in this study is available from the corresponding author upon reasonable request.

Acknowledgements

This work was partially supported by the National Natural Science Foundation of China (Grant No.: 62375266).

Author contributions

B.L. and M.Z. conceived the study and supervised the project; Y.X. is responsible for assisting in satellite mission planning; S.G. is responsible for the development of space lasers; Y.J. and B.Z. contributed to the temporal-coding architecture; J.Liao, J.Li, G.G., G.L., F.H., Y.Q., H.W. and H.Z. contributed to payload integration and calibration; J.H. and H.Y. contributed to the data analysis; D.S. and X.Y. contributed to the lasers development; all of the authors discussed the results and contributed to the manuscript.

Competing interests

The authors declare no competing interests.

References

[1] Neuenschwander, A. L. et al. Monitoring Earth's climate variables with satellite laser altimetry. *Nature Reviews Earth & Environment* **5**, 11-29 (2024).

[2] Csatho, B. M. et al. Laser altimetry reveals complex pattern of Greenland Ice Sheet dynamics. *Proceedings of the National Academy of Sciences* **111**, 18478-18483 (2014).

[3] Shepherd, A. et al. A reconciled estimate of ice-sheet mass balance. *Science* **338**, 1183-1189 (2012).

[4] Smith, B. et al. Pervasive ice sheet mass loss reflects competing ocean and atmosphere processes. *Science* **368**, 1239-1242 (2020).

[5] Dubayah, R. et al. The Global Ecosystem Dynamics Investigation: High-resolution laser ranging of the Earth's forests and topography. *Science of Remote Sensing* **1**, 100002 (2020).

[6] Dubayah, R. et al. Aboveground biomass density models for NASA's Global Ecosystem Dynamics Investigation (GEDI) lidar mission. *Remote Sensing of Environment* **270**, 112845 (2022).

[7] Burns, P. et al. Multi-resolution gridded maps of vegetation structure from GEDI. *Scientific Data* **11**, 899 (2024).

[8] Lefsky, M. A., Cohen, W. B., Parker, G. G. & Harding, D. J. Lidar remote sensing for ecosystem studies. *BioScience* **52**, 19-30 (2002).

[9] Campbell, J. B. & Wynne, R. H. *Introduction to Remote Sensing*. 5th edn. Guilford Press (2011).

[10] Schott, J. R. *Remote Sensing: The Image Chain Approach*. 2nd edn. Oxford University Press (2007).

[11] Rees, W. G. *Physical Principles of Remote Sensing*. 3rd edn. Cambridge University Press (2013).

[12] Wehr, A. & Lohr, U. Airborne laser scanning—an introduction and overview. *ISPRS Journal of Photogrammetry and Remote Sensing* **54**, 68-82 (1999).

[13] Shan, J. & Toth, C. K. *Topographic Laser Ranging and Scanning: Principles and Processing*. CRC Press (2008).

[14] Baltsavias, E. P. Airborne laser scanning: basic relations and formulas. *ISPRS Journal of Photogrammetry and Remote Sensing* **54**, 199-214 (1999).

[15] Zwally, H. J. et al. ICESat's laser measurements of polar ice, atmosphere, ocean, and land. *Journal of Geodynamics* **34**, 405-445 (2002).

[16] Schutz, B. E., Zwally, H. J., Shuman, C. A., Hancock, D. & DiMarzio, J. P. Overview of the ICESat mission. *Geophysical Research Letters* **32**, L21S01 (2005).

[17] Harding, D. J. & Carabajal, C. C. ICESat waveform measurements of within-footprint topographic relief and vegetation vertical structure. *Geophysical Research Letters* **32**, L21S10 (2005).

[18] Blair, J. B. & Hofton, M. A. Modeling laser altimeter return waveforms over complex vegetation using high-resolution elevation data. *Geophysical Research Letters* **26**, 2509-2512 (1999).

[19] Kirmani, A. et al. First-photon imaging. *Science* **343**, 58-61 (2014).

[20] Shin, D. et al. Photon-efficient imaging with a single-photon camera. *Nature Communications* **7**, 12046 (2016).

[21] Rapp, J. & Goyal, V. K. A few photons among many: unmixing signal and noise for photon-efficient active imaging. *IEEE Transactions on Computational Imaging* **3**, 445-459 (2017).

[22] Tachella, J. et al. Real-time 3D reconstruction from single-photon lidar data using plug-and-play point cloud denoisers. *Nature Communications* **10**, 4984 (2019).

[23] Li, Z.-P. et al. Single-photon computational 3D imaging at 45 km. *Photonics Research* **8**, 1532-1540 (2020).

[24] Wu, J. et al. Ultrafast time-of-flight 3D LiDAR. *Nature Photonics* **14**, 221-226 (2020).

[25] Markus, T. et al. The Ice, Cloud, and land Elevation Satellite-2 (ICESat-2): science requirements, concept, and implementation. *Remote Sensing of Environment* **190**, 260-273 (2017).

[26] Neumann, T. A. et al. The Ice, Cloud, and Land Elevation Satellite-2 mission: a global geolocated photon product derived from the Advanced Topographic Laser Altimeter System. *Remote Sensing of Environment* **233**, 111325 (2019).

[27] Martino, A. J. et al. The Advanced Topographic Laser Altimeter System (ATLAS) for NASA's Ice, Cloud and land Elevation Satellite-2 (ICESat-2). *IEEE Aerospace Conference* (2019).

[28] NASA Earthdata. Advanced Topographic Laser Altimeter System (ATLAS). NASA Earthdata Instrument Documentation.

[29] National Snow and Ice Data Center. ICESat-2: NASA Ice, Cloud, and land Elevation Satellite-2 mission documentation. NSIDC.

[30] Sun, X. et al. Space lidar developed at the NASA Goddard Space Flight Center: the first 20 years. *IEEE Journal of Selected Topics in Applied Earth Observations and Remote Sensing* **6**, 1660-1675 (2013).

[31] Santavicca, D. F. Scaling up single-photon detector arrays. *Nature Photonics* **17**, 120-121 (2023).

[32] Oripov, B. G. et al. A superconducting nanowire single-photon camera with 400,000 pixels. *Nature* **622**, 730-734 (2023).

[33] Bruschini, C., Homulle, H., Antolovic, I. M., Burri, S. & Charbon, E. Single-photon avalanche diode imagers in biophotonics: review and outlook. *Light: Science & Applications* **8**, 87 (2019).

[34] Habib, A. F., Kersting, A. P., Bang, K. I. & Lee, D.-C. Alternative methodologies for LiDAR system calibration. *Remote Sensing* **2**, 874-907 (2010).

[35] Schenk, T. & Csathó, B. Fusion of lidar data and aerial imagery for a more complete surface description. *International Archives of Photogrammetry and Remote Sensing* **34**, 310-317 (2002).